

LETTERS

A genetically encoded photoactivatable Rac controls the motility of living cells

Yi I. Wu^{1,3}, Daniel Frey⁴, Oana I. Lungu^{1,2,3}, Angelika Jaehrig^{1,3}, Ilme Schlichting⁴, Brian Kuhlman^{2,3} & Klaus M. Hahn^{1,3}

The precise spatio-temporal dynamics of protein activity are often critical in determining cell behaviour, yet for most proteins they remain poorly understood; it remains difficult to manipulate protein activity at precise times and places within living cells. Protein activity has been controlled by light, through protein derivatization with photocleavable moieties¹ or using photoreactive small-molecule ligands². However, this requires use of toxic ultraviolet wavelengths, activation is irreversible, and/or cell loading is accomplished via disruption of the cell membrane (for example, through microinjection). Here we have developed a new approach to produce genetically encoded photoactivatable derivatives of Rac1, a key GTPase regulating actin cytoskeletal dynamics in metazoan cells^{3,4}. Rac1 mutants were fused to the photoreactive LOV (light oxygen voltage) domain from phototropin^{5,6}, sterically blocking Rac1 interactions until irradiation unwound a helix linking LOV to Rac1. Photoactivatable Rac1 (PA-Rac1) could be reversibly and repeatedly activated using 458- or 473-nm light to generate precisely localized cell protrusions and ruffling. Localized Rac activation or inactivation was sufficient to produce cell motility and control the direction of cell movement. Myosin was involved in Rac control of directionality but not in Rac-induced protrusion, whereas PAK was required for Rac-induced protrusion. PA-Rac1 was used to elucidate Rac regulation of RhoA in cell motility. Rac and Rho coordinate cytoskeletal behaviours with seconds and submicrometre precision^{7,8}. Their mutual regulation remains controversial⁹, with data indicating that Rac inhibits and/or activates Rho^{10,11}. Rac was shown to inhibit RhoA in mouse embryonic fibroblasts, with inhibition modulated at protrusions and ruffles. A PA-Rac crystal structure and modelling revealed LOV–Rac interactions that will facilitate extension of this photoactivation approach to other proteins.

Recent NMR studies revealed the mechanism of a protein light switch in *Avena sativa* phototropin1 (refs 6, 12): a flavin-binding LOV2 domain interacts with a carboxy-terminal helical extension (J α) in the dark. Photon absorption leads to formation of a covalent bond between Cys 450 and the flavin chromophore, causing conformational changes that result in dissociation and unwinding of the J α helix. We fused the complete LOV2–J α sequence (404–547) to the amino terminus of a constitutively active Rac1, anticipating that the LOV domain in its closed conformation would block the binding of effectors to Rac1, and that light-induced unwinding of the J α helix would release steric inhibition, leading to Rac1 activation (Fig. 1a). Sampling of different junctional sequences in pull-down assays revealed that connecting Leu 546 of LOV2–J α to Ile 4 of Rac1 led to substantial reduction in Rac1 binding to its effector PAK (Fig. 1b and Supplementary Fig. 1a). To ensure that the photoactivatable Rac1 would induce no dominant-negative effects and that its activity would not be subject to upstream regulation, mutations were introduced to

abolish GTP hydrolysis and diminish interactions with nucleotide exchange factors, guanine nucleotide dissociation inhibitors (Q61L) and GTPase activating proteins (E91H and N92H) (Supplementary Fig. 2 and Supplementary text ‘Characterization of Rac1 constructs’). This resulted in the photoactivatable analogue of Rac1 (PA-Rac1) used in the following studies. Pull-down assays showed that PA-Rac1 has greatly reduced affinity for its effector protein PAK in the dark, as does a PA-Rac1 construct containing a light-insensitive LOV2 mutation (C450A)¹³. Effector binding was restored in a PA-Rac1 construct containing a LOV2 mutant (I539E)¹⁴ which mimics the unfolded ‘lit state’ (Fig. 1b and Supplementary Fig. 1b). Isothermal titration experiments indicated that the dark and lit state mutants of PA-Rac1 differed tenfold in effector binding (200 nM versus 2 μ M) (Supplementary Fig. 3 and Supplementary Table 1), with lit state effector affinity similar to that of native Rac¹⁵.

Activation of PA-Rac1 was examined in HeLa cells expressing a YFP fusion of PA-Rac1 to gauge expression level. The cells remained quiescent when illuminated with wavelengths longer than flavin absorbance (515, 568 or 633 nm, data not shown), but within seconds after switching to 458 nm, lamellipodial protrusions and membrane ruffles appeared around the cell edges (Fig. 1c and Supplementary Movie 1). To show that this effect was due to PA-Rac1, kymograms were used to quantify maximum protrusion length; irradiation of PA-Rac1 elicited protrusions that were four times as long as those seen in cells expressing either LOV domain alone or the light-insensitive PA-Rac1(C450A) mutant (Supplementary Fig. 4). An important advantage of PA-Rac1 is its ability to control precisely the subcellular location of Rac activation. We first examined this in mouse embryo fibroblasts (MEFs) stably expressing PA-Rac1, and cultured without serum to minimize cell activity before irradiation. Irradiation of 20- μ m spots at the cell edge generated large protrusions clearly localized next to the point of irradiation (Fig. 1d and Supplementary Movie 2). Repeated irradiation led first to ruffles and then to protrusion. YFP–actin, YFP–PAK and YFP–Arp3 revealed actin polymerization at the edge of the Rac-induced protrusions with associated translocation of downstream effectors, and induction of localized PAK phosphorylation was shown by immunostaining (Supplementary Figs 5 and 6 and Supplementary Movies 3 and 4). Movement of a laser spot to different positions led to cessation of ruffling or protrusion at the initial irradiation position and new activities appearing where the laser spot was brought to rest (HeLa cells, Supplementary Movie 5), demonstrating reversible activation. In MEF cells, more prone to movement than HeLa cells, complex shape changes were produced by ‘painting’ the cell with the laser spot (Supplementary Movie 6). The area of protrusions in MEF cells was dependent on light dosage, indicating the valuable ability to control the level of Rac1 activation (Supplementary Fig. 7). PA-Rac1 diffusion was analysed using fluorescence recovery after photobleaching (FRAP) and using PA-Rac1 tagged with photoactivatable GFP¹⁶ (Supplementary

¹Department of Pharmacology, ²Department of Biochemistry and Biophysics, and ³Lineberger Comprehensive Cancer Center, University of North Carolina, Chapel Hill, North Carolina 27599, USA. ⁴Department of Biomolecular Mechanisms, Max Planck Institute for Medical Research, Jahn-Strasse 29, 69120 Heidelberg, Germany.

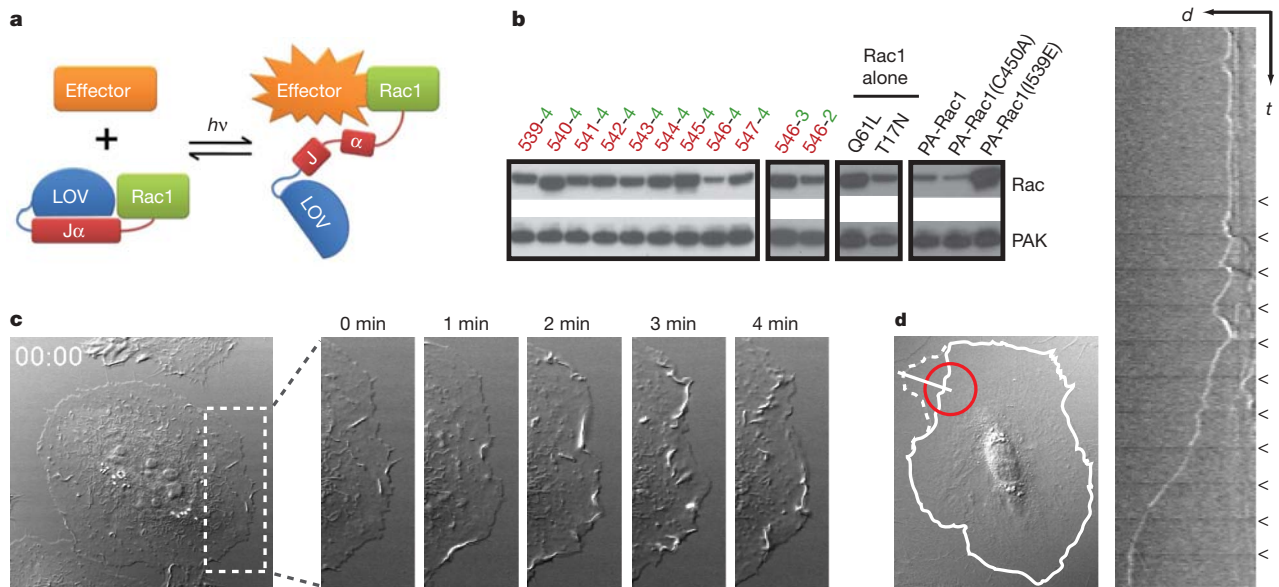


Figure 1 | Engineering and *in vivo* characterization of a photoactivatable Rac1 (PA-Rac1). **a**, Cartoon representation of PA-Rac1 design. *hν*, irradiation. **b**, Pull down of PA-Rac1 constructs with PAK in the dark. Truncations of LOV and Rac at their linkage point were tested: 539–547 in red, terminal amino acid of J α ; 2–4 in green, first residue of Rac1. 546–4 showed the strongest inhibition. PA-Rac1, 546–4 Q61L/E91H/N92H; PA-Rac1(C450A), light-insensitive mutant; PA-Rac1(I539E), lit state mutant. Pull down by constitutively active (Q61L) and dominant negative (T17N) mutants are included for comparison with PA-Rac1. **c**, Whole-cell

irradiation of a HeLa cell expressing PA-Rac1 (minutes after irradiation, DIC, short axis of box = 20 μ m). **d**, Spatial control of Rac1 activity. A 20- μ m circle (red) was irradiated every 60 s in serum-starved MEF cells. Solid line, cell border at time 0; dotted line, 10 min after initial light pulse. Little movement of the cell border was detected, except adjacent to the point of irradiation. The kymograph (taken using white line, 20 μ m), shows the initial formation of ruffles after each pulse, followed by protrusion (arrowheads indicate irradiation pulses).

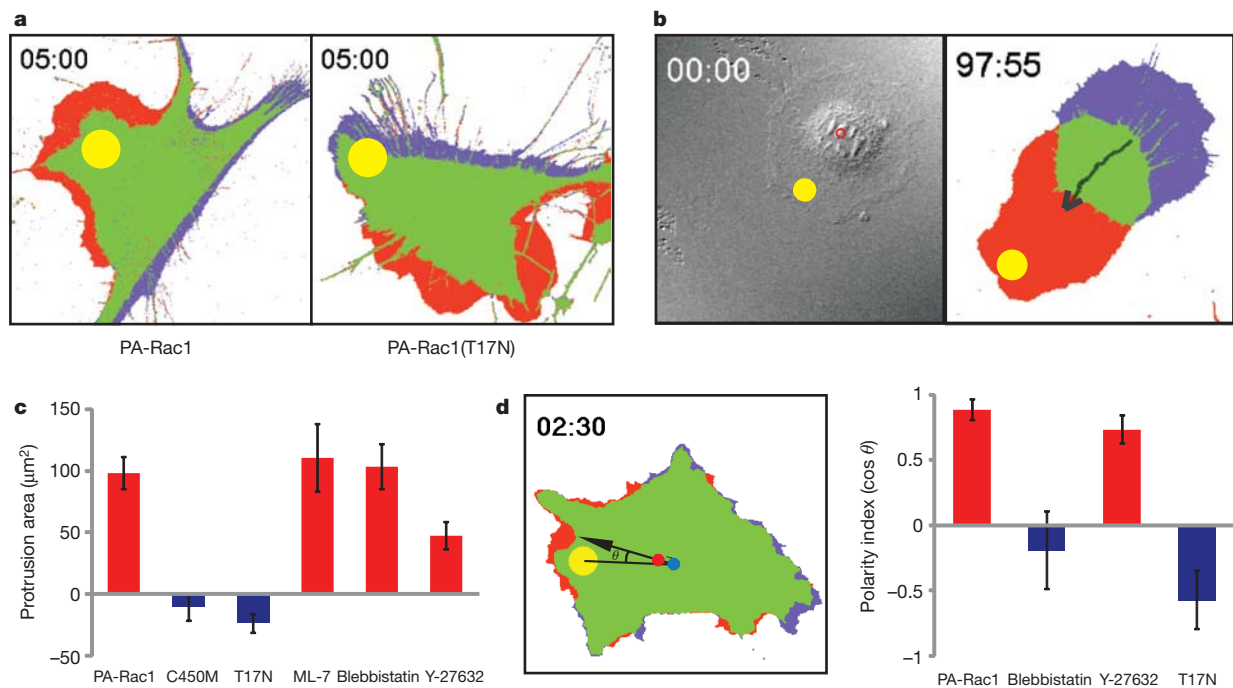


Figure 2 | Localized activation or inactivation of PA-Rac1 induces myosin-dependent migration. **a**, Protrusion/retraction map after a single pulse of activating illumination. MEFs expressing PA-Rac1 (left) generated protrusions at the site of irradiation (red) and retraction at the opposite side of the cell (blue) (in all 50 cells studied). Irradiation of the dominant-negative T17N mutant of PA-Rac1 (right) produced retraction near the point of irradiation, with protrusion in area(s) other than the site of irradiation (in all 25 cells studied). **b**, Repeated activation of PA-Rac1 at the cell edge induces directional migration. (MEF, 2-min intervals, average 0.8 μ m movement per pulse, $n = 6$.) **c**, Localized activation of PA-Rac1 in the

presence of ML-7 (MLCK inhibitor, 1 μ M), blebbistatin (myosin II ATPase inhibitor, 1 μ M) or Y-27632 (ROCK inhibitor, 10 μ M). Protrusions analysed as in panel **a**. **d**, Effect of myosin or ROCK inhibition on the ability of Rac1 to specify the direction of movement. The cosine of the angle between two lines (from the irradiation spot to the cell centroid at time 0, from the centroid at time 0 to the centroid at the end of the experiment) indicated how much the cell deviates from the direction specified by local irradiation. For **c**, **d**, $n > 25$; means \pm 95% confidence intervals; throughout Fig. 3 irradiation at 458 nm, spot diameter = 10 μ m; time shown is in minutes and seconds.

Fig. 8 and Supplementary Movies 7 and 8), indicating that PA-Rac1 diffuses more slowly than cytosolic proteins, probably because it is membrane bound ($10\text{-}\mu\text{m}$ spot, FRAP $D = 0.55\text{ }\mu\text{m}^2\text{ s}^{-1}$ or $t_{1/2} = 12.1\text{ s}$; PA-GFP $t_{1/2} = 14.6\text{ s}$). The half-life of dark recovery for PA-Rac1 was determined to be 43 s at room temperature. Simulation using this value indicated that, for two adjacent $10\text{-}\mu\text{m}$ spots, the unirradiated spot will achieve at most 7.5% the activation of the irradiated region (Supplementary Fig. 8c). Together these studies validate PA-Rac1 as a robust, genetically encoded and reversible caged protein effective in living cells.

We used PA-Rac1 to ask whether localized Rac activation is sufficient to specify cell polarity. In MEF cells, activating Rac1 at one spot near the cell edge not only generated protrusion locally, but also produced retraction on the opposite side of the cell (Fig. 2a and Supplementary Movie 9). To test whether this cross-cell coordination was due to a gradient of Rac1 activity, we fused the LOV domain to a dominant-negative mutant of Rac1 using the same linkage as in PA-Rac1. Irradiation of this PA-Rac1(T17N) led to nearby retraction rather than protrusion, and now generated protrusion in other areas of the cell (Fig. 2a and Supplementary Movies 10 and 11). The ability of Rac1 alone to control polarized movement was confirmed by repeated irradiation at the cell edge, which could be used to produce prolonged cell movement by generating consistent coordinated extension and retraction (MEF cells, Fig. 2b and Supplementary Movie 12; HEK293 cells, Supplementary Movie 13). In contrast to MEF and HEK293 cells, HeLa cells showed localized protrusion but

could not be induced to retract or move simply by activating Rac (Supplementary Movie 3), indicating that Rac-induced motility is subject to modulation by other pathways.

PA-Rac1 enabled control of Rac1 activity without the prior cellular compensation seen with other techniques, that is, mutation or altered expression. Using this advantage, we examined the role of myosin, a key mediator of actin-based contractility, in Rac-induced motility. Global inhibition of myosin activity using the myosin ATPase inhibitor blebbistatin or the myosin light chain kinase inhibitor ML-7 strongly affected Rac's ability to specify the direction of cell movement, but minimally affected Rac-induced protrusion (Fig. 2c, d). Myosin may mediate Rac's control of directionality through induction of tail retraction¹⁷, contraction of the cell cortex to direct protrusive force¹⁸, or coupling of actin to adhesions differently at the front and rear¹⁹. In contrast, inhibition of PAK was found to strongly affect Rac-induced protrusion (Supplementary Fig. 9). Inhibition of the Rho-activated kinase ROCK using Y27632 suggested a role for ROCK in Rac-induced protrusion, but these results must be interpreted with caution owing to known off-target effects²⁰.

Where and how Rac regulates Rho *in vivo* remains largely unknown; this was examined by using PA-Rac1 together with a RhoA biosensor⁸. Localized activation of Rac1 led to immediate inhibition of RhoA, and this inhibition spread outwards from the irradiated spot (Fig. 3a and Supplementary Movie 14). This was not simply an artefact of biosensor photobleaching, as irradiating the photoinactive C450M mutant (Fig. 2c) of PA-Rac1 led to localized

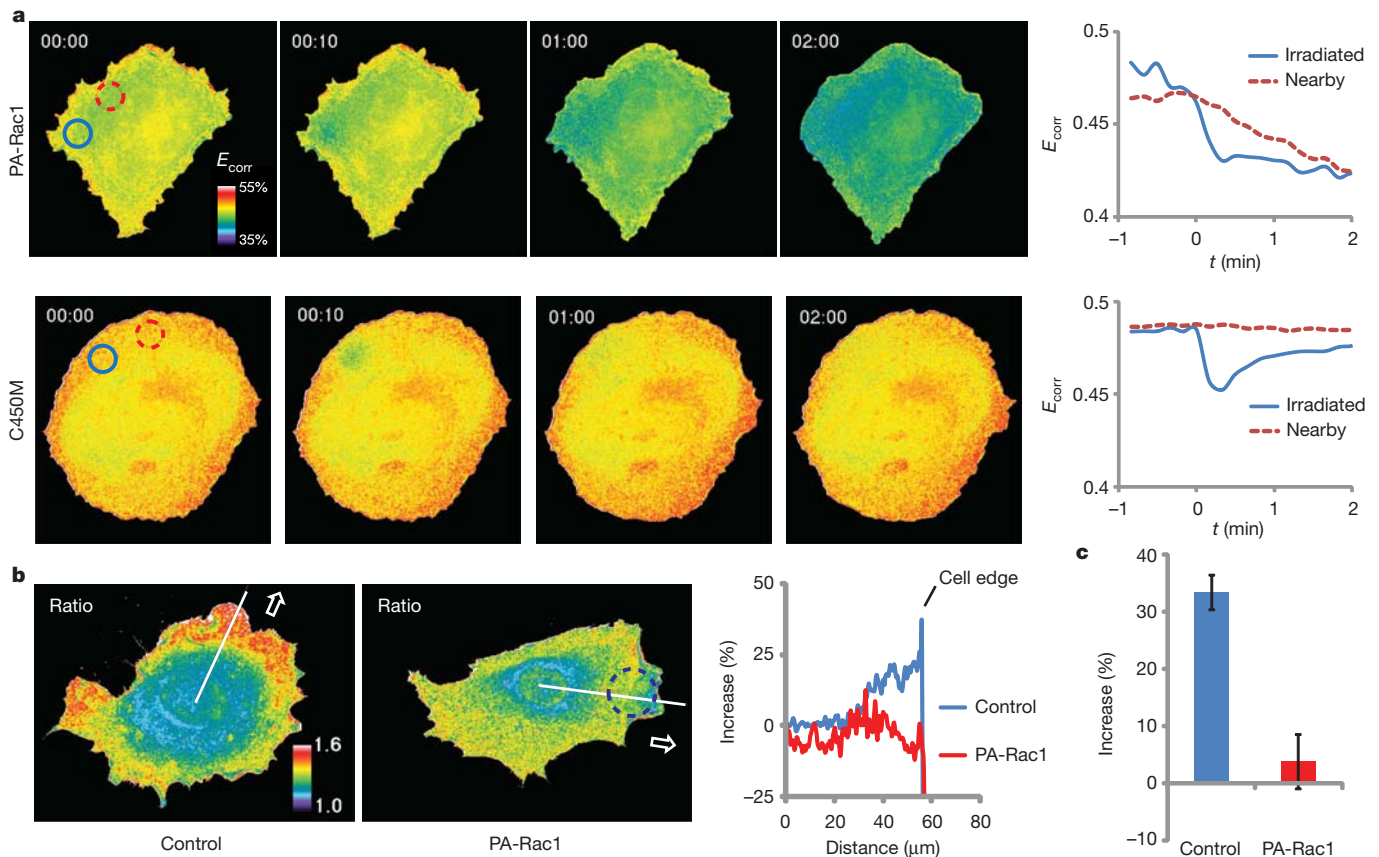


Figure 3 | Inhibition of RhoA by PA-Rac1. **a**, HeLa cells expressing RhoA biosensor and either PA-Rac1 or its C450M photoinactive mutant, illuminated in a $10\text{-}\mu\text{m}$ circle with a single pulse of 473-nm light. Changes in the FRET efficiency (E_{corr}) of the RhoA biosensor, indicative of RhoA activation, are shown in pseudocolour and as plots of average FRET efficiency within the irradiated circle (blue) and a nearby circle (red). In the PA-Rac1 cells, the irradiated spot showed bleaching of the biosensor followed by a relatively constant level of reduced RhoA activity. The nearby spot showed no bleaching, but a gradual decrease in RhoA activity reaching

the low level achieved in the irradiated spot ($n = 3$ cells). In the control cells (C450M), the biosensor returned to near initial activation readouts after bleaching, and no change was seen in the nearby spot ($n = 3$ cells). Time shown is in minutes and seconds. **b**, RhoA activation in constitutive pseudopods^{8,21} versus pseudopods induced by PA-Rac1 (473 nm, $20\text{-}\mu\text{m}$ circle shown, Supplementary Movie 15). **c**, The bar graph shows the per cent increase in biosensor FRET/CFP ratio in the region $1\text{-}\mu\text{m}$ from the cell edge versus the mean of the flat region at the left of the line scan. Means \pm 95% confidence intervals, 18 lines from 6 cells per bar.

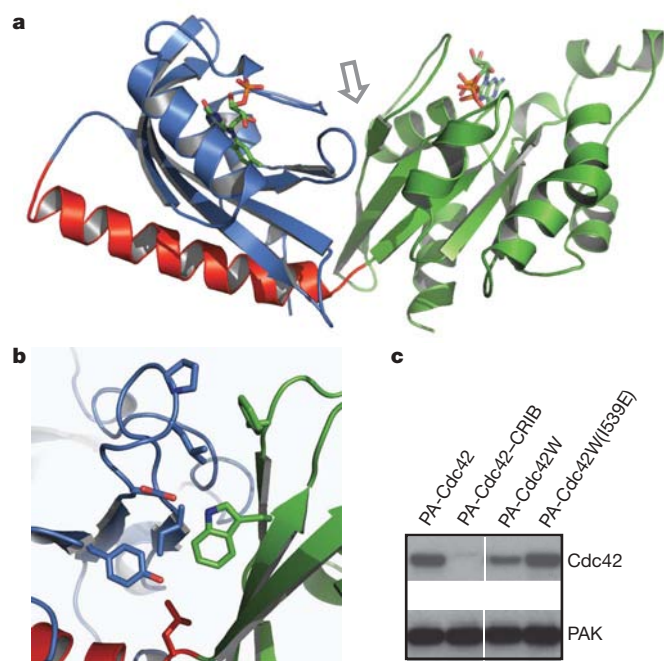


Figure 4 | Crystallization and structural modelling of PA-Rac1. **a**, Dark state crystal structure of PA-Rac1. Blue, LOV domain; red, $J\alpha$ helix; green, Rac1. **b**, Interacting residues at the LOV–Rac interface (arrow in panel **a**), including Trp 56. **c**, Mutating Cdc42 to include the Trp involved in stabilizing the LOV2–Rac1 interaction substantially improved LOV inhibition of Cdc42. Lane 1, PA-Cdc42; linking LOV to Cdc42 using the same truncations that produced good inhibition for Rac does not inhibit Cdc42–PAK binding. Lane 2, PA-Cdc42–CRIB; covalently linking the CRIB domain of PAK to PA-Cdc42 blocks PAK binding. Lane 3, PA-Cdc42(F56W) (PA-Cdc42W); introduction of the tryptophan substantially improves LOV inhibition of Cdc42 binding to PAK. Lane 4, lit state mutant of PA-Cdc42(F56W) (PA-Cdc42W(I539E)), showing that Cdc42 inhibition is sensitive to the lit/dark state of the LOV domain. Supplementary Movie 16 and Supplementary Fig. 14 demonstrate the ability of PA-Cdc42(F56W) to produce filopodia and protrusions in living cells.

biosensor photobleaching and recovery, but no prolonged local inhibition or wave of inhibition (Fig. 3a). There were marked differences between constitutive MEF protrusions and protrusions induced by pulsed PA-Rac1 irradiation. In contrast to constitutive protrusions, RhoA activity was greatly reduced in protrusions induced by PA-Rac (Fig. 3b). Inhibition of RhoA seems to be compartmentalized or controlled kinetically when Rac is activated in the context of normal motility, as both active Rac and active Rho are seen at the leading edge^{7,8,21}. PA-Rac activation led to large ruffles moving from the site of irradiation rearwards towards the nucleus (Supplementary Movie 15), suggesting that Rac regulates rearwards membrane flow. In control experiments, irradiation of cells expressing the photoinactive C450M mutant did not produce polarized ruffling or show reduced RhoA activity (data not shown).

To understand the structural basis of the PA-Rac1 switch for future application to other proteins, we performed Rosetta structure prediction simulations²² on several LOV2–Rac1 constructs, and determined high-resolution crystal structures of photoactive and inactive PA-Rac1 in the dark state. The crystal structures confirmed that the LOV domain occludes effector binding in the dark state (Fig. 4a and Supplementary Table 2). LOV- $J\alpha$ adopted a closed conformation that superimposes with the recently published structure of isolated LOV- $J\alpha$ (ref. 23). In the conformational ensemble predicted by simulations of the dark state, the effector binding site of Rac was sterically blocked by the LOV domain in a majority of the low-energy models (Supplementary Tables 3–5 and Supplementary Figs 10–13). Consistent with pull-down assays (Fig. 1b and Supplementary Fig. 1a), adding or removing even one residue from the connection

between LOV and Rac resulted in conformational ensembles with exposed effector binding sites. In the dark state, Rac was seen to form an extensive interface with the LOV domain (Fig. 4b), occluding Rac binding interactions. Given the substantial structural similarity between Rac1 and Cdc42, we hypothesized that the linkage used for PA-Rac1 failed to reduce Cdc42 binding to PAK (Fig. 4c and Supplementary Fig. 1d). Using the PA-Rac1 crystal structure as a template, a model was built of the Cdc42–LOV dark state. At the interface between Rac and LOV a hydrophobic cluster is formed between residues Phe37 and Trp56 from Rac and Leu422, Pro423, Ile428, Tyr508 and Leu546 from LOV. Consistent with this being a weak, non-evolved interaction, most of the hydrogen-bonding potential at the Rac–LOV interface is satisfied by buried and partially buried water molecules instead of inter-domain hydrogen bonds (Fig. 4b). This interface model was used to identify a mutation to Cdc42, F56W, at the Rac–LOV interface, that was predicted to stabilize the dark state. Pull-down assays showed that this mutation substantially improves dark-state inhibition of PAK binding, and produces differential affinity for Cdc42 effector in the dark versus the lit state (Fig. 4d). In living cells, irradiation of the mutated PA-Cdc42 led to production of filopodia and in some cases protrusions and/or ruffles, consistent with Cdc42 induction of filopodia and activation of Rac²⁴ (Supplementary Fig. 14 and Supplementary Movie 16). These results argue that PA-Rac1 can serve as a blueprint for engineering other caged GTPases.

We have engineered genetically encoded photoactivatable Rac1 analogues that enable precise spatial and temporal control of Rac activity in live cells, with reversible activation at 458 or 473 nm. Localized Rac activation or deactivation was sufficient to generate polarized cell movement. Rac could be activated without cellular compensation, enabling us to probe the role of myosin and PAK in Rac-mediated motility. Spatially regulated Rac inhibition of Rho was demonstrated in living cells. Structural studies indicate that a non-evolved interaction at the Rac–LOV interface can be engineered to cage other GTPases. This study and other recent work^{25–28} show that coupling genetically encoded light-modulated domains to other proteins provides a versatile new route to control protein activities in living cells.

METHODS SUMMARY

Imaging experiments were conducted on an Olympus FluoView 1000 laser scanning confocal microscope and an Olympus IX81-ZDC inverted microscope. Biosensor imaging was performed as previously described^{8,29}. Simultaneous biosensor imaging and activation of PA-Rac was achieved using a MAG Biosystems FRAP-3D add-on (Photometrics) for galvanometer control of laser position.

Full Methods and any associated references are available in the online version of the paper at www.nature.com/nature.

Received 21 March; accepted 30 June 2009.

Published online 19 August 2009.

- Goeldner, M. & Givens, R. *Dynamic Studies in Biology: Phototriggers, Photoswitches and Caged Biomolecules* (Wiley-VCH, 2005).
- Fortin, D. L. *et al.* Photochemical control of endogenous ion channels and cellular excitability. *Nature Methods* **5**, 331–338 (2008).
- Raftopoulou, M. & Hall, A. Cell migration: Rho GTPases lead the way. *Dev. Biol.* **265**, 23–32 (2004).
- Ridley, A. J. *et al.* Cell migration: integrating signals from front to back. *Science* **302**, 1704–1709 (2003).
- Christie, J. M., Salomon, M., Nozue, K., Wada, M. & Briggs, W. R. LOV (light, oxygen, or voltage) domains of the blue-light photoreceptor phototropin (nph1): binding sites for the chromophore flavin mononucleotide. *Proc. Natl Acad. Sci. USA* **96**, 8779–8783 (1999).
- Harper, S. M., Neil, L. C. & Gardner, K. H. Structural basis of a phototropin light switch. *Science* **301**, 1541–1544 (2003).
- Kraynov, V. S. *et al.* Localized Rac activation dynamics visualized in living cells. *Science* **290**, 333–337 (2000).
- Pertz, O., Hodgson, L., Klemke, R. L. & Hahn, K. M. Spatiotemporal dynamics of RhoA activity in migrating cells. *Nature* **440**, 1069–1072 (2006).
- Burridge, K. & Wennerberg, K. Rho and Rac take center stage. *Cell* **116**, 167–179 (2004).

10. Ridley, A. J., Paterson, H. F., Johnston, C. L., Diekmann, D. & Hall, A. The small GTP-binding protein rac regulates growth factor-induced membrane ruffling. *Cell* **70**, 401–410 (1992).
11. Sander, E. E., ten Klooster, J. P., van Delft, S., van der Kammen, R. A. & Collard, J. G. Rac downregulates Rho activity: reciprocal balance between both GTPases determines cellular morphology and migratory behavior. *J. Cell Biol.* **147**, 1009–1022 (1999).
12. Yao, X., Rosen, M. K. & Gardner, K. H. Estimation of the available free energy in a LOV2-J α photoswitch. *Nature Chem. Biol.* **4**, 491–497 (2008).
13. Salomon, M., Christie, J. M., Knieb, E., Lempert, U. & Briggs, W. R. Photochemical and mutational analysis of the FMN-binding domains of the plant blue light receptor, phototropin. *Biochemistry* **39**, 9401–9410 (2000).
14. Harper, S. M., Christie, J. M. & Gardner, K. H. Disruption of the LOV-J α helix interaction activates phototropin kinase activity. *Biochemistry* **43**, 16184–16192 (2004).
15. Thompson, G., Owen, D., Chalk, P. A. & Lowe, P. N. Delineation of the Cdc42/Rac-binding domain of p21-activated kinase. *Biochemistry* **37**, 7885–7891 (1998).
16. Patterson, G. H. & Lippincott-Schwartz, J. A photoactivatable GFP for selective photolabeling of proteins and cells. *Science* **297**, 1873–1877 (2002).
17. Vicente-Manzanares, M., Zareno, J., Whitmore, L., Choi, C. K. & Horwitz, A. F. Regulation of protrusion, adhesion dynamics, and polarity by myosins IIA and IIB in migrating cells. *J. Cell Biol.* **176**, 573 (2007).
18. Burridge, K. & Chrzanowska-Wodnicka, M. Focal adhesions, contractility, and signaling. *Annu. Rev. Cell Dev. Biol.* **12**, 463–518 (1996).
19. Giannone, G. *et al.* Lamellipodial actin mechanically links myosin activity with adhesion-site formation. *Cell* **128**, 561–575 (2007).
20. Davies, S. P., Reddy, H., Caivano, M. & Cohen, P. Specificity and mechanism of action of some commonly used protein kinase inhibitors. *Biochem. J.* **351**, 95–105 (2000).
21. Kurokawa, K. & Matsuda, M. Localized RhoA activation as a requirement for the induction of membrane ruffling. *Mol. Biol. Cell* **16**, 4294–4303 (2005).
22. Rohl, C. A., Strauss, C. E., Misura, K. M. & Baker, D. Protein structure prediction using Rosetta. *Methods Enzymol.* **383**, 66–93 (2004).
23. Halavaty, A. S. & Moffat, K. N- and C-terminal flanking regions modulate light-induced signal transduction in the LOV2 domain of the blue light sensor phototropin 1 from *Avena sativa*. *Biochemistry* **46**, 14001–14009 (2007).
24. Nobes, C. D. & Hall, A. Rho, rac, and cdc42 GTPases regulate the assembly of multimolecular focal complexes associated with actin stress fibers, lamellipodia, and filopodia. *Cell* **81**, 53–62 (1995).
25. Lee, J. *et al.* Surface sites for engineering allosteric control in proteins. *Science* **322**, 438–442 (2008).
26. Moglich, A., Ayers, R. A. & Moffat, K. Design and Signaling Mechanism of Light-Regulated Histidine Kinases. *J. Mol. Biol.* **385**, 1433–1444 (2008).
27. Strickland, D., Moffat, K. & Sosnick, T. R. Light-activated DNA binding in a designed allosteric protein. *Proc. Natl Acad. Sci. USA* **105**, 10709–10714 (2008).
28. Leung, D. W., Otomo, C., Chory, J. & Rosen, M. K. Genetically encoded photoswitching of actin assembly through the Cdc42-WASP-Arp2/3 complex pathway. *Proc. Natl Acad. Sci. USA* **105**, 12797–12802 (2008).
29. Hodgson, L., Shen, F. & Hahn, K. M. Biosensors for characterizing the dynamics of Rho family GTPases in living cells. *Curr. Protoc. Cell Biol.* (in the press).

Supplementary Information is linked to the online version of the paper at www.nature.com/nature.

Acknowledgements We are grateful for help and constructs from W. Briggs, K. Moffat, A. Tripathy, G. Bokoch and K. Jacobson. Diffraction data were collected at the Swiss Light Source, beamline X10SA, Paul Scherrer Institute, Villigen, Switzerland. We thank the Dortmund-Heidelberg team for data collection, and A. Pauluhn and M. Fuchs for their support in setting up the beamline. This research was supported by the American Heart Association (Y.I.W.) and the National Institutes of Health (K.M.H. grants GM057464 and GM64346).

Author Contributions Y.I.W. initiated the project, demonstrated the validity of caging Rac with LOV, and performed the studies of Rac biological function. He was assisted by A.J. in cloning and protein expression. D.F. and I.S. determined and analysed the crystal structures. O.I.L. performed molecular modelling and isothermal calorimetry studies under the direction of B.K. K.M.H. coordinated the study and wrote the final version of the manuscript, based on contributions from all authors.

Author Information The structural coordinates of PA-Rac1 and its mutants have been submitted to the Protein Data Bank under accessions 2wkp (wild type), 2wkq (C450A) and 2wkr (C450M). Reprints and permissions information is available at www.nature.com/reprints. Correspondence and requests for materials should be addressed to K.M.H. (khahn@med.unc.edu) or Y.I.W. (yiwu@med.unc.edu).

METHODS

DNA cloning. The cDNA encoding the LOV2 domain of *Avena sativa* (oat) Phototropin1 (404–546), including the C-terminal helical extension ($J\alpha$), was a gift from K. Moffat. Chimaeric fusion constructs consisting of LOV2- $J\alpha$ fused to Rac1 or Cdc42 were generated using an overlapping PCR approach so that precise junctional sequences could be engineered without being limited by restriction sites. These included truncations/extensions of the LOV2- $J\alpha$ C terminus (539–547), the N terminus (2–4) of the GTPases, or insertions of designed Schellman caps (KEAGADQI and KELKEAGADQI)¹. The QuickChange (Stratagene) protocol was used to introduce additional point mutations, including C450A or C450M, and I539E to mimic the dark and lit state of the LOV domain, respectively. PA-Rac1 was constructed as follows: LOV2- $J\alpha$ (404–546)–Rac1(4–192)/Q61L/E91H/N92H. These constructs were inserted into a pTriEx (Novagen) vector for transient expression in mammalian cells as well as in bacteria. For crystallization, C-terminally truncated PA-Rac1 (Δ 181–192) was subcloned into the pQE-30 vector (Qiagen). Fluorescent proteins mVenus², mCherry³ and mPA-GFP⁴ were inserted at the N terminus of the LOV domain with a short GSGS linker to monitor expression and subcellular localization. After initial characterization, PA-Rac1 with different fluorescent protein tags was subcloned into pBabe-TetCMV vector for retroviral production and establishment of stable MEF Tet-Off cell lines. High-fidelity Pfu Turbo DNA polymerase (Stratagene) was used in PCR reactions and all plasmids were verified by DNA sequencing.

Pull-down assay of effector binding. mVenus-tagged LOV2- $J\alpha$ and Rac1 fusion constructs were coexpressed with Flag-tagged PAK1 in HEK293 (LinXE) cells by transient transfection using Fugene 6 (Roche). The cells were lysed in 50 mM Tris pH 7.5, 150 mM NaCl and 1% Triton X-100 (lysis buffer) with addition of EDTA-free protease inhibitor cocktail (Roche). After brief centrifugation, the supernatants were incubated with Flag/M2-agarose (Sigma) followed by washes with lysis buffer, and elution with lysis buffer containing 200 μ g ml⁻¹ 3 \times Flag peptide (Sigma). All procedures were done at 4 °C under red light, facilitated using Handee spin columns (Pierce). The purified protein complexes as well as cell lysates were fractionated on 4–12% NuPAGE gels (Invitrogen) followed by western blot analysis using antibodies against fluorescent protein (JL-8, Clontech) and PAK (N-20, Santa Cruz). Myc pull-down experiments were performed similarly using anti-Myc agarose and Myc peptide (Sigma) to investigate the interaction of PA–Rac constructs with p50RhoGAP.

Expression, purification and characterization of proteins used for crystallization. C-terminal truncated PA-Rac1 (Δ 181–192) was expressed in *Escherichia coli* strain XL-10 Gold (Stratagene) at 30 °C overnight. All purification steps were done under yellow light at 4 °C. Cells were lysed in 20 mM Tris pH 8.5, 50 mM NaCl, 5 mM MgCl₂ and 2 mM 2-mercaptoethanol. Protein was purified with a Ni-NTA-FastFlow column (Qiagen) exploiting the N-terminal 6 \times His tag. The elution was dialysed against 10 mM Tris pH 8.5, 20 mM NaCl, 5 mM MgCl₂ and 2 mM 2-mercaptoethanol. The protein was bound to a MonoQ column (GE Healthcare) and eluted with a linear gradient (0–250 mM NaCl in 50 CV). Fractions containing the protein were concentrated (30 kDa cutoff, Millipore) and further purified by Superose 6 gel filtration chromatography (GE Healthcare, 10 mM Tris pH 8.5, 20 mM NaCl, 5 mM MgCl₂ and 2 mM DTE). Before crystallization the protein was concentrated to 10 mg ml⁻¹ (30 kDa cutoff, Millipore). All proteins were characterized spectroscopically. PA-Rac1 showed reversible light/dark conversion. The dark recovery rate of PA-Rac1 was measured as described previously⁵. The inactive C450A mutation showed no effect on light illumination whereas truncated C450M (Δ 181–192) was prone to aggregation on light illumination and, therefore, no data for light/dark conversion could be measured.

Crystallization. Crystallization was carried out under dimmed red light at 20 °C. PA-Rac1 and its C450A and C450M mutants were crystallized using the vapour diffusion method by mixing equal volumes of protein (10 mg ml⁻¹) and precipitant solution (100 mM calcium acetate/100 mM sodium cacodylate/12% (w/v) PEG 8000 or 4% (w/v) PEG 4000/100 mM potassium chloride). Yellow pencil-shaped crystals appeared overnight and grew to a final size of 50 \times 50 \times 1,000 μ m³ in a week. To avoid photoactivation, crystal handling was done by shielding the microscope light bulb with a 2-mm-thick RG630 filter (ITOS). Before cooling the crystals in liquid nitrogen they were transferred stepwise to precipitant solution supplemented with 20% (v/v) ethylene glycol for cryoprotection.

Data collection and structure determination. Diffraction data were collected at the X10SA beamline (Swiss Light Source) under standard cryogenic settings. Data were reduced using the XDS suite⁶ (Supplementary Table 2) and the structure was solved by molecular replacement⁷ using subsequentially 2V0U⁸ and 1MH1⁹ as the initial models. During several rounds of refinement with PHENIX¹⁰ and manual model building in COOT¹¹, FMN, GTP, Mg²⁺, Ca²⁺

and solvent molecules were included in the model. Structures were validated using MOLPROBITY¹² and PROCHECK¹³ (see Supplementary Table 2 for final statistics).

Structural modelling for linker optimization. The Rosetta program^{14,15} was used to predict the dark state structure of LOV2–Rac1 based on the solved crystal structures of dark state LOV2⁸ (Protein Data Bank (PDB) code 2V0U) and Rac1⁹ (PDB code 1MH1). Structure prediction simulations were performed on LOV2–Rac1 545–4, 546–4 and 547–4 constructs. In these simulations, the torsion angles of the residues connecting the two proteins were optimized with Monte Carlo sampling. Using the Rosetta domain assembly protocol¹⁶, we first applied 1,000 Φ and Ψ backbone torsion angle movements of up to 180° each to three residues connecting LOV2 to Rac1 in a low-resolution representation. Small backbone torsion angle moves of up to 4° were then performed on a high-resolution representation of LOV2–Rac1, followed by a global repacking of all side-chain rotamers. After every 15 cycles of small moves and repacking, further repacking was restricted to the rotamers at the interface and next to the LOV2–Rac1 linkers. This sequence of refinement was repeated for a total of 150 cycles. Next, we adopted a series of small moves, global rotamer repacking, as well as backbone minimization within 5 residues of the LOV2–Rac1 linker for high-resolution optimization cycles. After every ten cycles, only rotamers at the interface and next to the LOV2–Rac1 linkers were repacked. A total of 100 such high resolution optimizations were used to generate models, which were further scored using Rosetta's energy function. One-thousand models, each representing a different folding trajectory, were generated per construct from simulations using the domain assembly protocol.

The complex structure of Rac3 and the CRIB domain of PAK4 (PDB code 2OV2) was used to model the interaction of CRIB-containing effectors with LOV2–Rac1 constructs. The crystal structure of Rac1⁹ (PDB 1MH1) was superimposed onto the complex structure by mapping the C α atoms of Rac1 onto those of Rac3. This derived complex structure was then superimposed onto the LOV2–Rac1 models to create model–CRIB complexes. Side-chain rotamers at the interface of each complex were optimized using rotamer repacking¹⁷. These complexes were scored using the Rosetta energy function. A low-scoring model–CRIB complex indicated the model could bind CRIB, whereas a high-scoring model–CRIB complex indicated clashes between atoms of the model and the CRIB domain, resulting in reduced binding.

Models generated in a simulation were grouped into clusters according to their pairwise root mean square deviation (r.m.s.d.). The r.m.s.d. (in Å) of the C α atom positions of each model from all other models in the simulation was calculated. Those models falling within a radius of 3 Å r.m.s.d. from each other were grouped into a cluster. A cluster member representing the centre of each cluster was chosen.

Isothermal titration calorimetry. Dark and lit state mimetics of PA-Rac1, C450A and I539E were cloned into a pTriEx vector with an N-terminal six histidine tag. Residues 65–150 of PAK1, comprising the extended CRIB domain, were cloned into a pET23 vector, with a C-terminal 6xhistidine tag. All proteins were expressed in *E. coli* strain BL21(DE3) cells (Stratagene) at 16 °C overnight in the dark. Cells were lysed in 50 mM sodium phosphate pH 7.0, 300 mM NaCl and 5 mM MgCl₂. Proteins were purified under yellow light using TALON Metal Affinity Resin (Clontech) and eluted with 150 mM imidazole at pH 7.0. The proteins were dialysed against 50 mM sodium phosphate, 150 mM NaCl, 7.15 mM 2-mercaptoethanol, 5 mM MgCl₂ and 1% glycerol. Protein concentrations were quantified based on the estimated molar extinction coefficients (280 nm) of the corresponding polypeptides or the reported molar extinction coefficient (447 nm) of LOV2-FMN, and were confirmed with SDS–PAGE followed by Coomassie staining.

ITC experiments were performed by injecting the dark state mutant C450A of PA-Rac1 (0.14 mM) or the lit state mutant I539E (0.13 mM) into the CRIB domain of PAK1 (10 μ M) using a Microcal VP-ITC calorimeter at 25 °C. Each titration consisted of 29 injections of 10 μ l of mutants of PA-Rac1. The baseline of each titration was determined and subtracted from all of the data points. Titration data for the heat change per injection were fitted to a one-site binding model using Origin software (OriginLab).

Cell culture. HeLa, HEK293 (ATCC) and parental MEF/3T3 Tet-Off cells (Clontech) were maintained in DMEM containing 10% FBS following the supplier's culturing instructions. Stable MEF lines were passaged with addition of 1 ng ml⁻¹ doxycycline, sufficient to suppress protein expression under the Tet-CMV promoter. Doxycycline was removed 24 h before live cell imaging. It was important to control expression level because small amounts of Rac activity from PA-Rac were apparently present before irradiation, as evidenced by increased ruffling at high expression levels. This was probably due to the equilibrium amount of active Rac present in the dark state. For constructs tagged with fluorescent proteins, expression level could be roughly approximated as proportional to brightness/unit area, enabling use of cells with similar expression.

Live cell microscopy. Cells for live cell imaging were seeded on coverslips coated with $5 \mu\text{g ml}^{-1}$ fibronectin in Ham's F-12K medium free of Phenol red and containing 2% fetal bovine serum (FBS). Coverslips were mounted in an Attofluor live cell chamber (Invitrogen) placed in a microscope stage with a heated stage adaptor (Warner). Initial characterization and photoactivation of PA-Rac1, diffusion studies by FRAP and PA-GFP, and protrusion/retraction analyses were carried out using an Olympus FluoView 1000 confocal scanning microscope system equipped with a $\times 60$ 1.42 NA oil objective and lasers at 405, 458, 488, 515, 568 and 633 nm. Fluorescence images were acquired using 0.1% power from a 30 mW multi-line Ar ion laser (Olympus, minimum power possible without introducing a neutral density filter) and scanned at $2 \mu\text{s}$ per pixel. The illumination used for photoactivation of PA-Rac1 was between 0.1% power for $10 \mu\text{s}$ and 1% power for 1 ms in a $10\text{-}\mu\text{m}$ spot, at 458 nm. A more precise measure of the light dose used for activation was obtained by measuring the power after the objective using a power meter (Thorlabs), as described in Supplementary Fig. 7.

Biosensor images were acquired using an Olympus IX81-ZDC microscope equipped with a CoolSNAP HQ2 14-bit camera (Photometrics) and ET-CFP/YFP filters (Chroma) as described previously^{18,19}. Band-pass and neutral density filters were switched using motorized filter wheels under computer control (Ludl). CFP, FRET and YFP images were acquired using a 100 W Hg arc lamp with a 3% ND filter for 500, 250 and 250 ms, respectively. FRET/CFP ratio images were calculated after shading correction, background subtraction, binary masking and image registration using MetaMorph and MatLab software as described previously^{18–20}.

Our imaging conditions, exposure times and filters resulted in a donor (ECFP) bleed-through factor (into the FRET channel) of 0.25 and an acceptor (Citrine) bleed-through factor of 0.07, using the previously described approach^{18–20}. The E-FRET calculation was used as a measure of apparent FRET efficiency of the RhoA biosensor, producing a G factor of 1.57. Photobleaching-corrected FRET efficiency (E_{corr}) images were processed based on acceptor photobleaching as previously described²¹. Imaging YFP acceptor fluorescence of the RhoA biosensor was carried out using band-pass filters 500/20 (excitation) and 545/30 (emission).

Simultaneous photoactivation and biosensor imaging was achieved using the FRAP-3D instrument (MAG Biosystems), an illumination system with galvanometer-driven laser positioning. A laser source at 473 nm was incorporated into the illumination pathway using beam-combining mirrors (Chroma, or a 94%/6% Magic Mirror from Olympus).

Immunocytochemistry. MEF cells expressing mVenus-PA-Rac were plated onto coverslips with etched grids (Bellco) that were coated with fibronectin as described above. The cells were locally irradiated at 473 nm through a $\times 20$ phase-contrast objective. Immediately after protrusions were induced, the cells were fixed in 3.7% formalin (Sigma), permeabilized in 0.2% Triton X-100, incubated with anti-phospho-PAK antibody (Cell Signaling), and finally incubated with Alexa Fluor 594-conjugated secondary antibody (Molecular Probes). The numbers on the etched-grid coverslips were used to locate the immunostained cells that had been previously irradiated.

Measurement of protrusion length. Protrusions were analysed by drawing up to 8 lines per cell, perpendicular to the cell border and at least 45 degree apart (a few lines were dropped because of cell junctions). More than 14 cells were analysed

for each construct. The line scans were analysed as kymographs, oriented as shown in Supplementary Fig. 4. The protrusion length was defined as the maximal distance of the membrane from the left hand border of the kymograph after irradiation minus the average distance of the cell border from the left hand edge of the kymograph before irradiation.

Fluorescence recovery after photobleaching (FRAP). MEF cells expressing mVenus-tagged PA-Rac1 were irradiated (515 nm, 10% power for $100 \mu\text{s}$) at a $10\text{-}\mu\text{m}$ spot using the Olympus FluoView1000 confocal scanning microscope and laser detailed above. The intensity of mVenus fluorescence was monitored (515 nm, 0.1% power for $2 \mu\text{s}$) before and after photobleaching at 2-s intervals. The intensity of fluorescence within the bleached spot was normalized against the integrated intensity of the entire cell. The data were plotted and fitted to a single-exponential decay to obtain $t_{1/2}$ (τ_D). A $t_{1/2}$ of 12.1 s and F_i (immobile fraction) of $18.6 \pm 0.6\%$ were obtained ($n = 26$). The diffusion coefficient ($D = 0.55 \mu\text{m}^2 \text{s}^{-1}$) was estimated using $D = \omega^2/4\tau_D$ (where ω is the radius of the circular bleached spot), assuming exclusively free lateral diffusion^{22,23}.

PA-GFP tracking. MEF cells expressing mPA-GFP-tagged PA-Rac1 were irradiated (405 nm, 6 mW diode laser, 10% power for $10 \mu\text{s}$) in a $10\text{-}\mu\text{m}$ spot to switch on PA-GFP. The fluorescence of PA-GFP was monitored using a 488-nm laser, acquiring an image every 2 s. The intensities of fluorescence within the irradiated spot and an adjacent spot of the same size were quantified and normalized against the entire cell. The decay of activated PA-GFP fluorescence was fitted to a single exponential decay, yielding a $t_{1/2}$ of 14.6 s.

Inhibitor studies. MEF cells expressing mVenus-tagged PA-Rac1 were incubated with $1 \mu\text{M}$ myosin II inhibitor blebbistatin, $1 \mu\text{M}$ MLCK inhibitor ML-7, or $10 \mu\text{M}$ ROCK inhibitor Y-27632 (Calbiochem). Cells underwent the cell shape changes previously described²⁴ and then reached a stable state within 30 min. After this cells were irradiated with the 458-nm laser at a $10\text{-}\mu\text{m}$ spot to induce PA-Rac activation.

Protrusion/retraction analysis. Fluorescence images of MEF cells expressing mVenus-tagged PA-Rac1 and its mutants were masked based on intensity thresholding to produce binary images. Regions of protrusion were isolated by subtracting the binary image at a given time point from that at time 0. Conversely the binary images of retraction were obtained. Areas not part of protrusions or retractions, those that overlapped the time 0 image, were obtained by subtracting the above two images from that at time 0. Each binary image was assigned a different colour: red, protrusion; blue, retraction; green, area overlapping with time 0; and white, background. These operations were carried out using MetaMorph software.

Polarity index calculation. To obtain the polarity index ($\cos\theta$) of the migrating MEF cells, x and y coordinates were obtained for the centroid before movement (x_0, y_0), the centroid after movement (x_1, y_1), and for the centre of the irradiation spot (x_2, y_2), using MetaMorph software. The cos and sin values of the angles were obtained using simple triangle calculations. First two angles were defined using an arbitrarily selected horizontal line $\theta_1 =$ angle between the arbitrary line and the line from (x_0, y_0) to (x_1, y_1), and $\theta_2 =$ angle between the arbitrary line and the line between (x_0, y_0) and (x_2, y_2). The cos used to characterize polarity (see main text and Fig. 2d) was obtained using the following formula: $\cos\theta = \cos(\theta_1 - \theta_2) = \cos\theta_1\cos\theta_2 + \sin\theta_1\sin\theta_2$.